



Steering charge kinetics in W₂C@C/TiO₂ heterojunction architecture: Efficient solar-light-driven hydrogen generation



Xin-Zheng Yue^a, Chuan-Qi Li^a, Zhong-Yi Liu^a, Sha-Sha Yi^{b,*}, De-Liang Chen^b, Feng Wang^c, Shuai-Hui Li^{a,*}

^a College of Chemistry and Molecular Engineering, Zhengzhou University, Zhengzhou, 450001, China

^b School of Materials Science and Engineering, Zhengzhou University, Zhengzhou, 450001, China

^c Henan Institutes of Advanced Technology, Zhengzhou University, 97 Wenhua Road, Zhengzhou, 450003, China

ARTICLE INFO

Keywords:

Photocatalytic
Hydrogen generation
Steer charge kinetics
TiO₂
W₂C@C

ABSTRACT

The constructing of functional materials with well-defined nanostructure, showing efficient charge separation and transportation properties, has been intensively and in depth investigated to fabricate catalysts for H₂ generation from solar-driven water reduction. Here we demonstrate that loading W₂C@C structure in which each W₂C nanoparticle (NP) is wrapped by carbon shell on surface of hollow TiO₂ microspheres (HTMs) can enhance the separation of photogenerated electron-hole pairs by building an internal electric field in W₂C@C/HTMs composite structure and act as the reaction active sites for water reduction. As expected, the optimized W₂C@C/HTMs construction exhibits the highest photocatalytic H₂ generation rate of 6.91 mmol h⁻¹ g⁻¹ under simulated solar light illumination, over 20 times larger than that of bare HTMs. The underlying mechanism has been investigated from the perspective of photochemistry and photophysics based on a series of characterization techniques, which suggests that W₂C@C can effectively steer the charge kinetics, maximizing the charge carriers' separation.

1. Introduction

Solar water splitting for hydrogen (H₂) generation with a semiconductor photocatalyst has been considered to be a potential and sustainable pathway toward novel renewable energy sources in the future, attracting particular attentions [1–3]. With the seminal discovery of TiO₂ photoelectrode for water reduction [4], the investigation of TiO₂-based materials for solar-driven H₂ production is of particular interest because of its suitable conduction band (CB) structure for proton reduction, chemical stability, earth abundance, and low toxicity [5]. However, TiO₂ also has some disadvantages. For example, it possesses a wide bandgap (3.0~3.2 eV) that only can absorb ultraviolet (UV) region of the solar spectrum (less than 5%), resulting in insufficient utilization of solar energy [5]. On the other hand, it suffers sluggish charge transfer kinetics resulted from its fast recombination of photogenerated electrons and holes. Therefore, various efficient strategies, including doping with foreign elements, decorating with cocatalysts, constructing heterojunctions with a second material, etc. have been adopted for optimization of TiO₂ architecture to enhance light harvesting ability and improve charge separation efficiency [6–9]. Among them, the construction of unique heterojunction nanostructures

has been demonstrated to be one of the most efficient techniques to suppress the charge recombination.

In this regard, we are keen to search an appropriate material to combine with TiO₂ for building the heterojunction architecture with matched energy band potentials. Because we know that, an internal electric field could be generally formed when two different materials come to contact on account of the redistribution of charge carriers [10], which gives a high driving force for charge transportation and separation. Recently, transition metal carbides, especially for tungsten carbide (W₂C) which is known as the promising electrocatalyst for hydrogen evolution reaction (HER) and acts as the alternative to platinum group metals, ascribing to its good characters, such as the similar electronic property to that of Pt, high chemical and electrochemical stability, low-cost, and so on [11,12]. Besides, generally, the carbon or graphene could be produced along with the formation of tungsten carbides [13,14], which can serve as charge-transport channel for electron and hole diffusion owing to the high mobility of its charge carriers. In this case, W₂C@C (W₂C nanoparticles (NPs) is wrapped by carbon (C) shell) is expected to couple with TiO₂ to construct heterojunction nanostructures, exhibiting boosted photocatalytic H₂ generation activity from water reduction.

* Corresponding authors.

E-mail addresses: yiss@zzu.edu.cn (S.-S. Yi), lishuahui@gs.zzu.edu.cn (S.-H. Li).

Here, we report the design and synthesis strategy of W₂C@C/HTMs (hollow TiO₂ microspheres) heterojunction architecture *via* a facile step-by-step process. By comparing with bare HTMs, this kind of structural photocatalyst not only can enhance the light harvesting capacity by the W₂C@C, but also accelerate the charge transfer rate, boost electron-hole pairs' separation, and provide abundant reactive sites for water reduction. Remarkably, the photocatalytic H₂ generation rate is sharply enhanced with W₂C@C decorating and achieves maximal value on specimen of 4W₂C@C/HTMs, reaching 6.91 mmol h⁻¹ g⁻¹ under solar light irradiation (21 times that of pristine HTMs).

2. Experimental section

2.1. Chemicals and reagents

All chemicals and reagents used were of analytical grade. Dicyanodiamide (C₂H₄N₄, ≥98.0%), sodium sulfate (Na₂SO₄, ≥99.0%), formaldehyde aqueous solution (HCHO, 37.0~40.0%), ethanol (CH₃CH₂OH, 75%), acetone (CH₃COCH₃, ≥99.5%), triethanolamine (C₆H₁₅NO₃, TEOA, ≥99.0%) and ammonium tungstate hydrate ((NH₄)₅H₅[H₂(WO₄)₆]·H₂O, ≥85.0~90.0%) were bought from Sinopharm Chemical Reagent Co., Ltd. Titanic sulfate (Ti(SO₄)₂, ≥96%), resorcinol (C₆H₆O₂, 99%), potassium hydroxide (KOH, 90%), glucose (C₆H₁₂O₆, 98.0%) and commercial Nafion 117 solution (DuPont, 5 wt%) were purchased from Aladdin Reagent Co., Ltd. Fluorine-doped tin oxide glass (F:SnO₂, FTO, <15 O sq⁻¹) was acquired from Zhuhai Kaivo Optoelectronic Technology Co., Ltd. Before experiment, the FTO (1 cm × 2.5 cm) was ultrasonically rinsed by sonication in acetone, ethanol and water, respectively, for 15 min and dried by an Ar stream. The deionized water (18.2 MΩ cm) used throughout all experiments was obtained by reverse osmosis followed by ion-exchange and filtration.

2.2. Synthesis of hollow TiO₂ microspheres (HTMs)

The HTMs were fabricated by a combination of hydrothermal method and carbonization process. With magnetic stirring, Ti(SO₄)₂ (0.5 g) and resorcinol (0.8 g) were firstly dissolved in 30 mL of deionized water. Then, formaldehyde aqueous solution (2 mL) was added into the above solution to achieve a homogeneous mixture, whereafter be transferred to the Teflon-lined stainless steel autoclave and heated at 85°C for 72 h. Subsequently, the collected precipitate was separated and washed with deionized water for five times, and dried in oven. Finally, the HTMs were achieved after being sintered for 3 h at 500°C in the furnace.

2.3. Synthesis of W₂C@C

The W₂C@C was synthesized *via* a simple high-temperature calcination process at 850°C for 3 h in Ar atmosphere, using the dicyanodiamide (0.2 g) and ((NH₄)₅H₅[H₂(WO₄)₆]·H₂O) (0.4787 g) as the raw materials.

2.4. Synthesis of W₂C@C/HTMs heterojunction

A wet-impregnation method was employed to synthesize the W₂C@C/HTMs hybrid. In a typical synthesis, 4 mg of W₂C@C and 100 mg of HTMs specimens were respectively dispersed in 25 mL deionized water by ultrasonication for 30 min. Then, a mixture was achieved by mingling above two solutions, which was kept under constant stirring at 80°C in oil bath for 5 h and following at 100°C until the solid precipitation was collected. Following, the obtained solid powers were annealed at 350°C for 2 h in Ar atmosphere at a ramp rate of 5°C min⁻¹. In such a whole process, the marked 4W₂C@C/HTMs hybrid was achieved as expected, wherein the weight ratio of W₂C@C and HTMs was 1:25. Similarly, the W₂C@C/HTMs composite specimens

with various W₂C@C contents (0.5, 1, 2, 6 and 8 wt%) were prepared by altering the weight of addition, which were labelled as 0.5W₂C@C/HTMs, 1W₂C@C/HTMs, 2W₂C@C/HTMs, 6W₂C@C/HTMs and 8W₂C@C/HTMs, respectively.

2.5. Characterization

X-ray photoelectron spectroscopy (XPS) measurements were performed on a Thermo VG Scientific ESCALAB 250 spectrometer using monochromatized Al K α excitation. All binding energies were calibrated by using C 1s (284.60 eV) as the reference. The crystal structure of the as-prepared samples were examined with powder X-ray diffraction (XRD) with a Rigaku D/Max-2550 diffractometer using Cu K α radiation ($\lambda = 1.54056 \text{ \AA}$) at 50 kV and 200 mA in the 2θ range of 10~80° at a scanning rate of 10° min⁻¹. The UV-vis diffuse reflectance spectra (UV-vis DRS) of the specimens were recorded using a UV-vis-NIR spectrophotometer (Shimadzu UV-3600) equipped with an integrating sphere, detecting absorption over the range of 300~800 nm. The steady-state photoluminescence (PL) emission spectra were performed at room temperature on a FLUOROMAX-4 under an excitation wavelength of 325 nm. The Brunauer-Emmett-Teller (BET) surface areas and pore volumes were analyzed on a Micromeritics ASAP 2020 sorptometer using adsorption data in the relative pressure (P/P₀) range of 0.05~0.25. The thermal gravimetric (TG) analyses were performed on NETZSCH STA 449F3 instrument by heating the samples to 800 °C at a rate of 10° min⁻¹. The field emission scanning electron microscope (FESEM) images were obtained with a JEOL JSM 6700 F electron microscope. The transmission electron microscopy (TEM), high-resolution TEM (HRTEM) images, a selected area electron diffraction (SAED), energy-dispersive X-ray (EDX) spectroscopy and scanning TEM-EDX spectrometry elemental mapping were conducted on a Tecnai G2 F20 TEM microscope (FEI Company). Raman spectra were measured on a micro-Raman spectrometer (LabRAM HR evolution, laser wavelength 390 nm). The ultraviolet photoelectron spectroscopy (UPS) spectra was recorded on a Thermo ESCALAB 250XI analyzer by using a monochromatic He I light source (21.22 eV), which was employed to calculate the valence band energy of the samples. The data were acquired with -5 V bias.

2.6. Photocatalytic H₂ generation reaction

The photocatalytic H₂ generation reaction was carried out at ambient temperature and atmospheric pressure in a glass reaction cell equipped with a quartz cover. In a typical process, 25 mg of photocatalyst was homogeneously dispersed into 100 mL of aqueous solution with 10 vol% (volume ratio) TEOA in the reaction cell by ultrasonication for 10 min. Because that the reaction was performed under the anaerobic condition, then the system should be vacuumed for 15 min to remove the dissolved oxygen before irradiation. Illumination was provided by a 300 W Xe lamp (CEL-HXF 300, 320 < λ < 780 nm, 178 mW cm⁻²) and a cooling water was used to stabilize the reaction temperature at 277 K. For visible-light-driven H₂ generation, a 300 W Xe lamp with a UV cutoff filter (λ ≥ 420 nm) was employed. A 0.4 mL of H₂ gas was intermittently collected and analyzed using an online gas chromatograph (GC-8A, Shimadzu Co., Japan, with N₂ as the carrier gas) equipped with an MS-5A column and a thermal conductivity detector (TCD). For long-time photocatalytic stability tests, the same processing parameters were adopted and a total number of 20 h was done for five cycles. For Pt/HTMs (weight percent of Pt is 1 wt%) test, Pt was loaded on the surface of HTMs through the in-situ photo-deposition method by using H₂PtCl₆ as the Pt source.

The apparent quantum efficiency (AQE) was measured over 4W₂C@C/HTMs specimen under monochromatic light irradiation provided by a 300 W Xe lamp with the band-pass filter of 365 nm. The AQE was calculated as the following Eq. (1) [15]:

$$\text{AQE}(\%) = \frac{N_1}{N_2} \times 100 = \frac{N_A \times M}{\frac{E \times \lambda}{hc}} \times 100 \quad (1)$$

where N_1 and N_2 represent the number of evolved H_2 molecules and the number of incident photons. N_A , h and c are the Avogadro's constant (6.02×10^{23} molecules mol^{-1}), Planck's constant (6.626×10^{-34} $\text{J}\cdot\text{s}$), and speed of light (3.0×10^8 m s^{-1}), respectively. M is the average H_2 generation rate (mol s^{-1}) and E is the power of lamp source (3.27 mW cm^{-2}).

2.7. Photo(electro)chemical measurements

To prepare working electrodes, 10 mg of photocatalysts (HTMs, $\text{W}_2\text{C}@C$ and $4\text{W}_2\text{C}@C/\text{HTMs}$), 375 μL of deionized water, 125 μL of ethanol and 50 μL of Nafion solution were mixed together to obtain the homogeneous suspension (also called ink solution). After that, 30 μL of ink solution was collected to drop-coated onto the clean-washed FTO glass and heated at 300 $^\circ\text{C}$ for 1 h in N_2 atmosphere. In typical photo (electro)chemical measurements, the as-prepared sample films, a Pt wire and Ag/AgCl (saturated KCl) were acted as the working electrodes, counter electrode and reference electrode, respectively, and all the experiments were carried out by employing an electrochemical analyzer (CHI760E Instruments). The electrolyte for all the electrochemical and photoelectrochemical (PEC) measurements was 1 M NaOH aqueous solution ($\text{pH} = 13.6$). For PEC reaction, a 300 W Xe lamp equipped with an AM 1.5 G solar simulator was used as the light source and the intensity was adjusted to 1 sun (100 mW cm^{-2}). The current-voltage (LSV) plots were conducted in dark condition and the current-time ($i-t$) curves were recorded at the applied potential of 0.2 V vs. Ag/AgCl under light on/off condition. The electrochemical impedance spectroscopy (EIS) measurements were performed under AM 1.5 G by applying an AC voltage with 5 mV amplitude in a frequency range from 100 kHz to 0.1 Hz under 0 V vs. Ag/AgCl condition. Open circuit potential (OCP) decay curves were conducted after turning off the light irradiation to analyze the charge decay behavior of the photocatalysts. The Mott-Schottky (M-S) plots were performed and recorded over an AC frequency of 0.5, 0.7 and 1 kHz in dark to determine the flat band potential of these materials as well as their characteristics of semiconductor types.

3. Results and discussion

3.1. Fabrication, morphology and component analysis of $\text{W}_2\text{C}@C/\text{HTMs}$ heterojunction nanostructures

The synthetic procedure of $\text{W}_2\text{C}@C/\text{HTMs}$ heterojunction nanostructures is designed and clearly illustrated in Fig. 1A. $\text{W}_2\text{C}@C$ and HTMs are fabricated based on the controlled thermal carbonization process and hydrothermal reaction strategies, respectively. Briefly, the dicyanodiamide ($\text{C}_2\text{H}_4\text{N}_4$) and ammonium tungstate hydrate ($(\text{NH}_4)_2\text{H}_5[\text{H}_2(\text{WO}_4)_6]\text{H}_2\text{O}$) were used as the raw materials to achieve $\text{W}_2\text{C}@C$ in Ar atmosphere at 850 $^\circ\text{C}$ for 3 h. To be specific, in the fabrication of $\text{W}_2\text{C}@C$, dicyanodiamide plays two significant roles that i) undergoes the carbonization process and ii) favors the deoxygenation of ammonium tungstate, achieving the in-situ growth of nanocarbon merged with the W_2C nanoparticles (NPs). Additionally, the carbon content (wt%) in specimen of $\text{W}_2\text{C}@C$ is analyzed based on the thermogravimetric (TG) measurement (Fig. S1), which is 36.38 wt%. Much more clearly, the transmission electron

microscopy (TEM) and high-resolution TEM (HRTEM) images of $\text{W}_2\text{C}@C$ specimen are shown in Fig. S2, wherein W_2C NPs are wrapped by C shell. Additionally, it is seen from the TEM and field emission scanning electron microscope (FESEM) images illustrated in Figs. S3 and S4 that HTMs are presented by the accumulation of small TiO_2 NPs, demonstrating the morphology of hollow microspheres with diameter of $\sim 3.5 \mu\text{m}$. What to expect: the hollow porous structure catalyst

processes high surface area, enhanced light harvesting as well as light scattering [16], thus improving the photocatalytic efficiency. Subsequently, a wet-impregnation technique is employed to synthesize the $\text{W}_2\text{C}@C/\text{HTMs}$ hybrid architecture, in which process the combination of HTMs and $\text{W}_2\text{C}@C$ is succeeded by the effect of physical absorption. Further, this interaction effect between HTMs and $\text{W}_2\text{C}@C$ could be strengthened through the thermal treatment at 350 $^\circ\text{C}$ for 2 h in Ar atmosphere. To gain in-depth insight into the hybrid nanostructure, we demonstrate TEM, HRTEM, scanning TEM-energy-dispersive X-ray (STEM-EDX) elemental mapping, selected area electron diffraction (SAED) and EDX characterizations of $\text{W}_2\text{C}@C/\text{HTMs}$. By comparing the TEM images of $\text{W}_2\text{C}@C/\text{HTMs}$ (Fig. 1B and C) with bare HTMs (Fig. S3A), it is difficult to prove the existence of $\text{W}_2\text{C}@C$ in visually, due to its low content. In $\text{W}_2\text{C}@C/\text{HTMs}$, it can be clearly seen that two different lattice fringes are measured and listed in Fig. 1D, in which the 0.26 nm can be assigned to the (002) plane of W_2C (Fig. 1D1) and the 0.35 nm corresponds to the (101) plane of TiO_2 (Fig. 1D2). In order to more directly identify the distribution of $\text{W}_2\text{C}@C$ in hybrid, STEM-EDX elemental mapping images are shown in Fig. 1E-I, revealing the homogeneous distribution of Ti, O, W and C in $\text{W}_2\text{C}@C/\text{HTMs}$. More importantly, this indicates that the nature of the heterostructure for $\text{W}_2\text{C}@C/\text{HTMs}$ could further be evidenced and inferred the presence of strong interaction between $\text{W}_2\text{C}@C$ and HTMs, which shows a vital role in facilitating the charge exchange and transfer in photocatalytic H_2 generation. Besides, it is also important to note that not only the SAED pattern (Fig. 1J) but also EDX analysis (Fig. 1K and S5) could confirm the co-existence of W_2C and HTMs in our target hybrid once again, in which the two sets of diffraction rings in SAED pattern can be assigned to W_2C and TiO_2 , respectively.

To get more insights on the phase component and surface chemical states, X-ray diffraction (XRD), Raman and X-ray photoelectron spectroscopy (XPS) are conducted. Fig. 2A firstly demonstrates the XRD patterns of HTMs, $\text{W}_2\text{C}@C$ and $4\text{W}_2\text{C}@C/\text{HTMs}$ specimens. For pure HTMs, a set of high intensity diffraction peaks are appeared and can be well match those of the crystal planes of anatase TiO_2 (JCPDS No. 21-1272). While for $\text{W}_2\text{C}@C$, the phases of W_2C (JCPDS No. 20-1315) and C (JCPDS No. 50-0926) could be simultaneously observed, suggesting the fact that carbon exists along with the formation of W_2C NPs, which result is well consistent with the TEM images (Fig. S2). No phases of W_2C and C are observed in specimen of $4\text{W}_2\text{C}@C/\text{HTMs}$, attributing to the low content of $\text{W}_2\text{C}@C$ in hybrid heterostructure. Raman spectrum of pristine HTMs displays the F_g modes of anatase TiO_2 at 148, 517, and 640 cm^{-1} , respectively, and the B_{1g} mode at 400 cm^{-1} (Fig. 2B) [17]. For the specimen of $\text{W}_2\text{C}@C$, the observed Raman peaks can be identified to W–O band (270 cm^{-1}) [18], W–C stretching modes (673 and 808 cm^{-1}) [13,19] as well as D and G bands (1351 and 1595 cm^{-1}) [20,21], respectively, which indicates the co-existence of W_2C and C. Here, the W–O band may originate from the surface oxidation of W_2C . While for hybrid catalyst $4\text{W}_2\text{C}@C/\text{HTMs}$, there of course shows Raman peaks for TiO_2 , W_2C and C. More interestingly, by comparing with pristine HTMs and $\text{W}_2\text{C}@C$, the Raman spectrum of $4\text{W}_2\text{C}@C/\text{HTMs}$ shows that blue-shifts are obviously observed in Raman shift region of 100~200 (inset of Fig. 2B) and G band, demonstrating strong interaction between HTMs and $\text{W}_2\text{C}@C$ [7], which greatly facilitates the charge transfer between them [14].

Next we illustrate the surface chemical states in $4\text{W}_2\text{C}@C/\text{HTMs}$ hybrid based on the characterization of XPS spectra, as shown in Fig. 2C-F and S6. The Ti 2p XPS spectrum of $4\text{W}_2\text{C}@C/\text{HTMs}$ reveals its normal state of Ti^{4+} , which could be confirmed by the binding energies (BEs) located at 464.97 and 459.27 eV, respectively, for $\text{Ti} 2p_{1/2}$ and $\text{Ti} 2p_{3/2}$ [6] (Fig. 2C). In the case of O 1s spectra in Fig. 2D, the XPS peak at BE of 530.57 eV could be indexed to oxygen bonding in $\text{Ti}-\text{O}-\text{Ti}$, while another one centered at 532.09 eV usually originates from the adsorbed hydroxyl on oxygen atom, that forms the O–H binding [8,22]. Further, the C 1s and W 4f high-resolution XPS profiles over $4\text{W}_2\text{C}@C/\text{HTMs}$ photocatalyst are displayed in Fig. 2E and F, which are used to

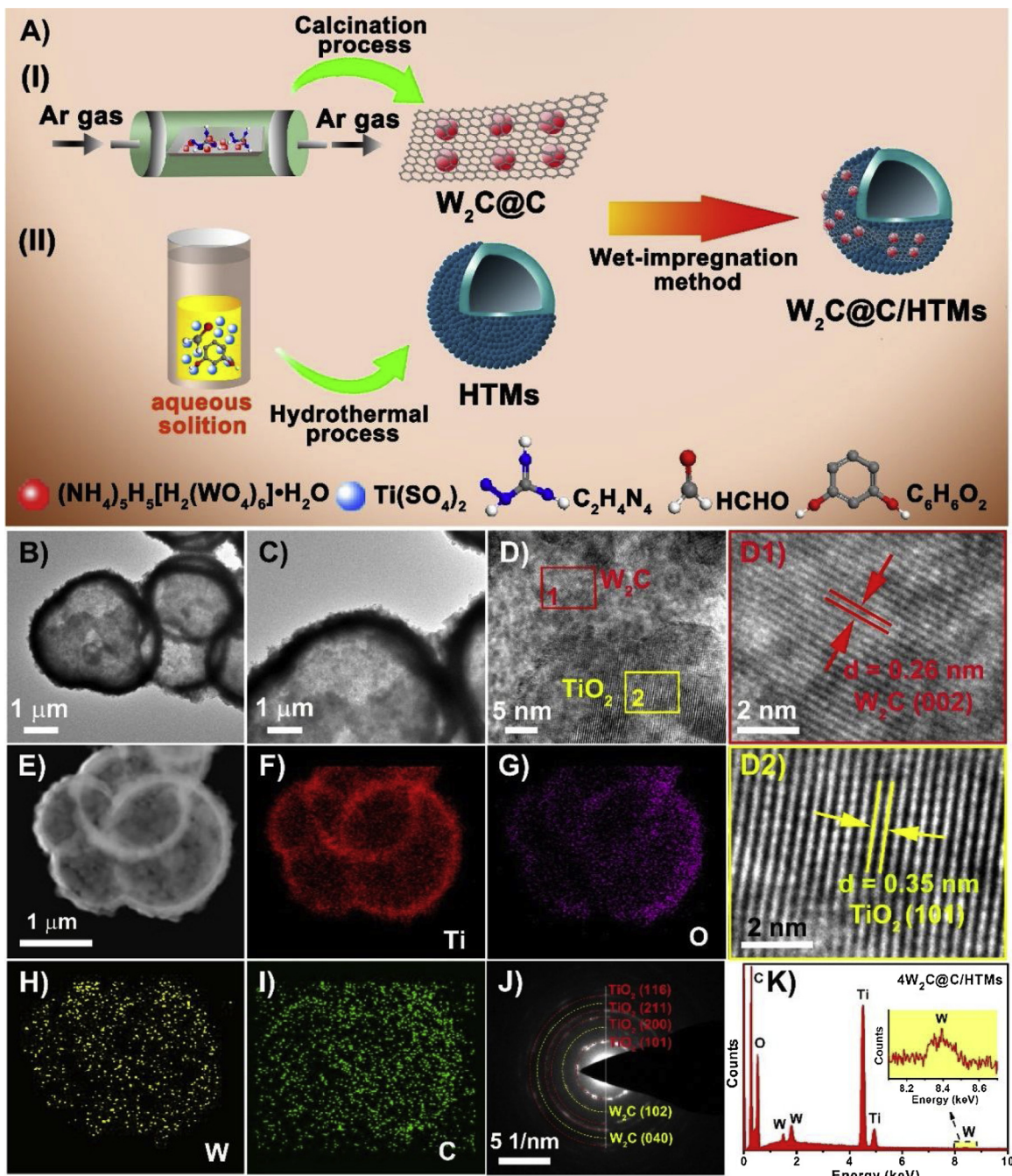


Fig. 1. Fabrication process and morphological characterizations of $4\text{W}_2\text{C}@\text{C}/\text{HTMs}$ heterojunction. (A) Schematic illustration of the synthesis of $4\text{W}_2\text{C}@\text{C}/\text{HTMs}$ heterojunction. (B,C) Low and high resolution TEM, and (D) HRTEM images over $4\text{W}_2\text{C}@\text{C}/\text{HTMs}$, respectively. (D1,D2) The enlarged views of the circled area in (D), which show the HRTEM images of W_2C and TiO_2 , respectively. (E) HAADF and (F–I) STEM-EDX elemental mapping (Ti, O, W and C elements) images, (J) SAED pattern, and (K) EDX spectrum of $4\text{W}_2\text{C}@\text{C}/\text{HTMs}$, respectively.

reveal the chemical environment of $\text{W}_2\text{C}@\text{C}$. As clearly to see in Fig. 2E that, apart from the C 1s peak centered at 284.60 eV (C–C bond), the peak associated with C–O bond locating at 285.63 eV [23] could also be found. This suggests that some tight coupling probably be presented between HTMs and $\text{W}_2\text{C}@\text{C}$ in $\text{W}_2\text{C}@\text{C}/\text{HTMs}$ hybrid. The W 4f profile shown in Fig. 2F demonstrates that $\text{W}_2\text{C}@\text{C}$ is indeed existed in our target composite. From the above results, it is evident that $\text{W}_2\text{C}@\text{C}/\text{HTMs}$ hybrid heterostructures have been successfully synthesized.

3.2. Highly efficient photocatalytic H_2 generation and optical characterization of $\text{W}_2\text{C}@\text{C}/\text{HTMs}$ nanostructures

The photocatalytic H_2 generation tests over a series of $\text{W}_2\text{C}@\text{C}/\text{HTMs}$ catalysts are conducted in aqueous solution containing sacrificial agent of triethanolamine (TEOA) under simulated solar light irradiation. A resulting histogram is demonstrated in Fig. 3A, which is employed to directly evaluate the H_2 generation rate. It is apparent that both HTMs and $\text{W}_2\text{C}@\text{C}$ alone all show very low activities in photocatalytic H_2 generation, whose rates are 0.32 and $0.07 \text{ mmol h}^{-1} \text{ g}^{-1}$, respectively, attributing to their fast recombination of photogenerated electrons and holes. It is surprising that after the low weight

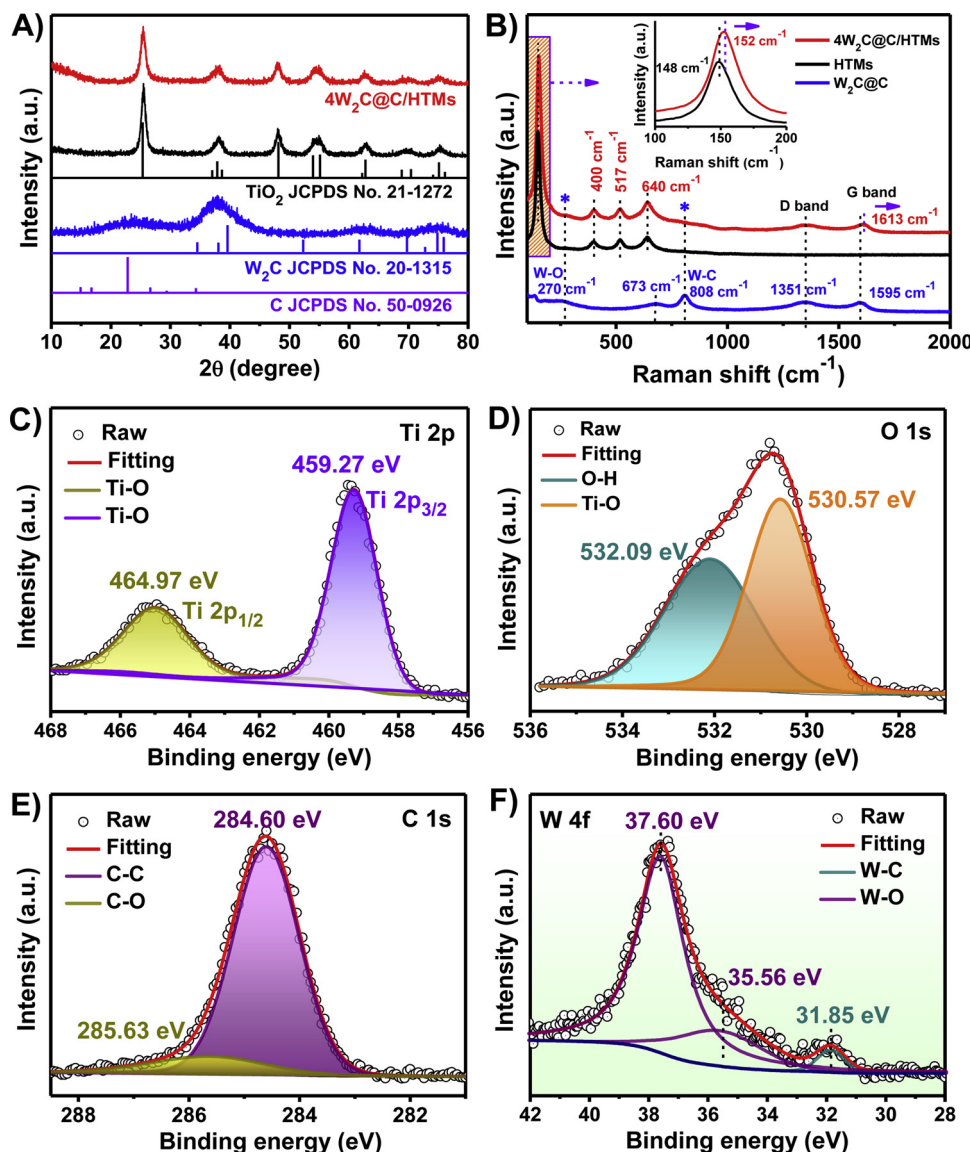


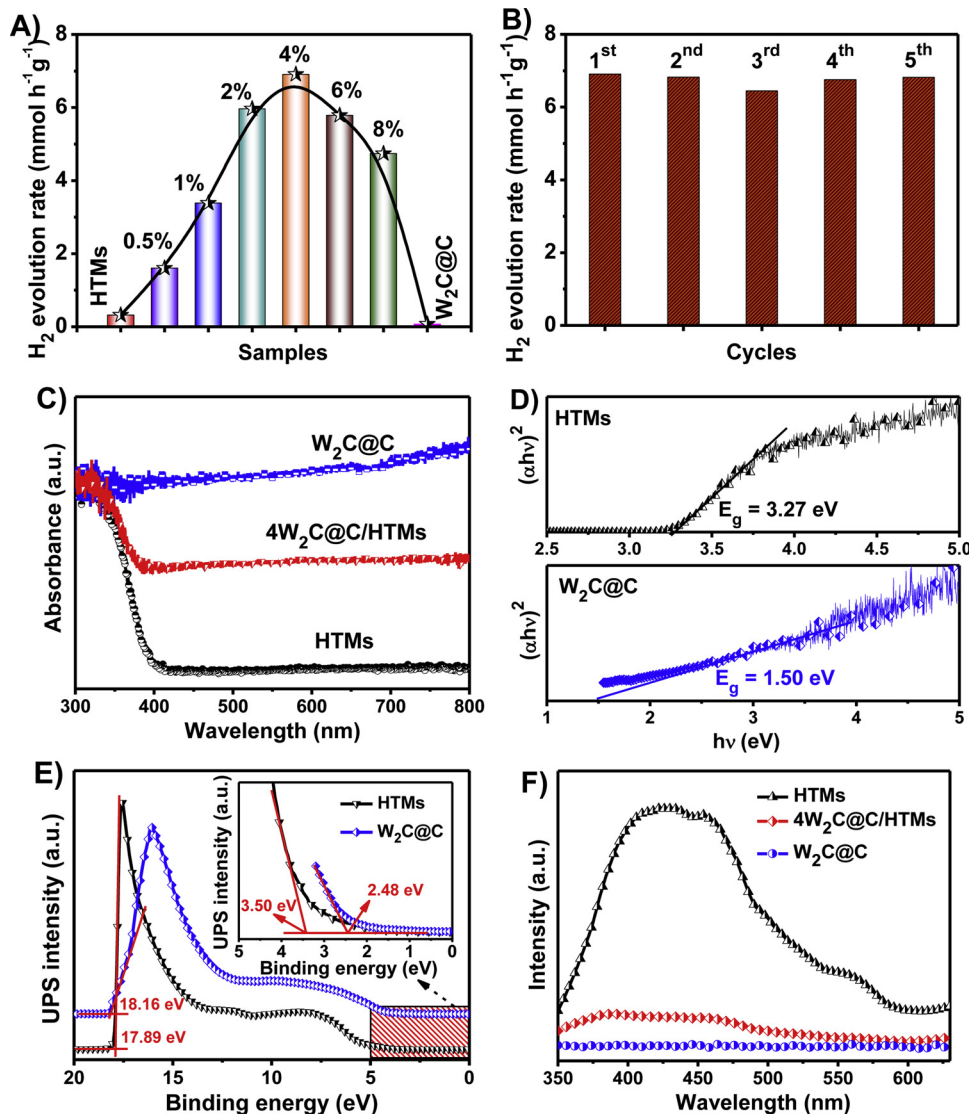
Fig. 2. Structural characterizations of 4W₂C@C/HTMs heterojunction hybrid. The typical (A) XRD and (B) Raman spectra of HTMs, W₂C@C, and 4W₂C@C/HTMs specimens. The high-resolution XPS spectra of (C) Ti 2p, (D) O 1s, (E) C 1s, and (F) W 4f for 4W₂C@C/HTMs specimen.

incorporation of W₂C@C into HTMs, the H₂ generation rate could be prominently boosted. Especially for 4W₂C@C/HTMs, it achieves the highest H₂ generation value of 6.91 mmol h⁻¹ g⁻¹, up to 21 times with respect to that of pristine HTMs. That is to say, the optimized loading weight content of W₂C@C is 4 wt%. This rate compares favorably to 1 wt% Pt/HTMs and most of the reported rates for TiO₂-based promising catalysts for photocatalytic H₂ generation, as shown in Fig. S7 and Table S1. Moreover, the apparent quantum efficiency (AQE) of 4W₂C@C/HTMs is recorded at $\lambda = 365$ nm to be 22%, which is higher than previously reported values [24–26]. To confirm W₂C plays the subjectivity role in the enhancement of activity, the photocatalytic activity of HTMs@C was conducted (Fig. S8), finding that it shows much lower activity than 4W₂C@C/HTMs. This result suggests that

W₂C in 4W₂C@C/HTMs does play the decisive effect in improvement of the photocatalytic performance. Additionally, as shown in Fig. 3B, the stable H₂ generation rate over 20 h (five cycles) of continuous operation under solar light irradiation is presented, which suggests that 4W₂C@C/HTMs processes good stability for water reduction. To better understand the photochemical stable behavior of 4W₂C@C/HTMs in long-time reaction, the cycling tests of photocatalytic H₂ generation over pristine HTMs and W₂C@C specimens are

also performed (Fig. S9). As a result, both HTMs and W₂C@C all show stable performance. Furthermore, the stable of 4W₂C@C/HTMs could also be proved by comparing its XRD and XPS results before and after photocatalytic reactions (Fig. S10 and S11). From these viewpoints, the heterojunction structure of W₂C@C/HTMs is successfully constructed and powerfully evidenced once again [27]. To further confirm the heterojunction is formed in W₂C@C/HTMs and that W₂C@C can indeed improve the separation of charge carriers, the photocatalytic performance for physical mixture of 4W₂C@C and HTMs is conducted for comparison, as shown in Fig. S12. As expected, the W₂C@C/HTMs heterojunction shows much higher activity than that of the physical mixture. Further, to explore the universality of W₂C@C acting as the cocatalysis effect, the photocatalytic H₂ generation rates of W₂C@C/CdS and W₂C@C/SrTiO₃ are also conducted (Fig. S13), whose results suggest that W₂C@C is a good cocatalyst when bonded with photoactive semiconductor materials.

To gradually explore the reasons for the improvement of photocatalytic performance when HTMs is decorated by W₂C@C, the light absorption of HTMs, W₂C@C and W₂C@C/HTMs hybrids are firstly measured by UV-vis diffuse reflectance spectra (UV-vis DRS) (Fig. 3C and S14). It can be seen that pure HTMs can only absorb UV light with



absorption edge around 390 nm, while for W₂C@C, the light absorption over the entire wavelength range of 300~800 nm could be observed (Fig. 3C), which may result from its exterior black color or the narrow band gap. Consequently, when decorated with slight amount of W₂C@C, a significant increase in the absorption under both UV and visible light regions for HTMs could be achieved (Fig. S14), indicating that W₂C@C could distinctly enhance the light harvesting ability of HTMs. While based on the photocatalytic result recorded on 4W₂C@C/HTMs under visible light irradiation (Fig. S12), we could deduce that the improved photocatalytic performance cannot be ascribed to the absorption enhancement in the visible light region. From the known UV-vis DRS of HTMs and W₂C@C, their energy band gaps (E_g) could be estimated by employing Kubelka-Munk function [28], as illustrated in Fig. 3D, the plots of (αhv)² as a function of the energy (hv) are displayed. Accordingly, the E_g values of HTMs and W₂C@C are obtained to be 3.27 and 1.50 eV, respectively. Further, in order to have a detailed analysis of the band structures over HTMs and W₂C@C, the ultraviolet photoelectron spectroscopy (UPS) measurements are carried out and their topmost valence bands (E_{VB}) are determined according to the following Eq.s (2) and (3) [29,30]:

$$E_{VB} (\text{vs. vacuum}) = - [\hbar\nu - (E_{cut} - E_F)] \quad (2)$$

$$E_{VB} (\text{vs. NHE}) = - 4.44 - E_{VB} (\text{vs. vacuum}) \quad (3)$$

where $\hbar\nu$ is the excitation energy of monochromatic He I light (21.22 eV), E_{cut} and E_F are the secondary electron cut-off edge (eV) and Fermi edge (eV) of the specimens, respectively. As it is shown in Fig. 3E, the E_{cut} of HTMs and W₂C@C are read to be 17.89 and 18.16 eV, respectively, and their E_F values are recorded as 3.50 and 2.48 eV. Then, the E_{VB} (vs. NHE) values of HTMs and W₂C@C are calculated to be 2.37 and 1.08 eV, respectively. As for the E_{CB}, it can be obtained by equation of E_{CB} = E_{VB} - E_g [31] as well as the known E_g values, that are -0.94 and -0.42 eV vs. NHE, respectively, for HTMs and W₂C@C. Another empirical method for examining the E_{CB} value of the semiconductor material is the Mott-Schottky (M-S) technique [29], which carries information about the flat band potential. As a consequence, the E_{CB} of HTMs and W₂C@C achieved from M-S plots (Fig. S15) are close to the values stemmed from UPS spectra, which indicates the valid band structures of HTMs and W₂C@C listed in Table S2.

Fig. 3F and S16 show the typical steady-state photoluminescence (PL) emission spectra of HTMs, W₂C@C and W₂C@C/HTMs heterojunction, which are applied to explore the behavior of charge carriers mainly the separation characteristic of photogenerated electron-hole pairs [32]. In contrast, the PL intensity of 4W₂C@C/HTMs is significantly quenched with respect to pure HTMs, which suggests that carrier-separation efficiency in hybrid is remarkably improved. These results give a good explanation that the existing heterojunction at

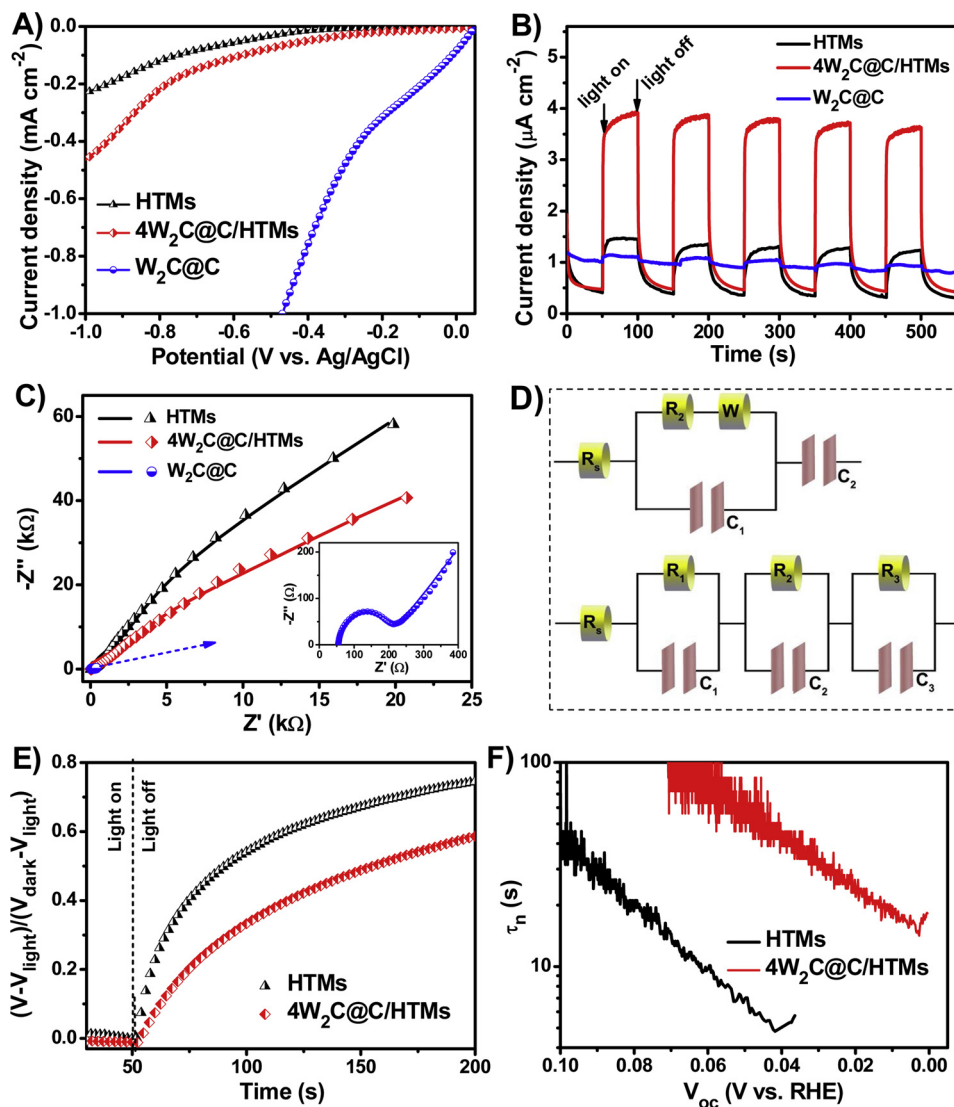


Fig. 4. Electrochemical and photoelectrochemical characterizations. (A) The current-voltage (LSV) characteristics of HTMs, $W_2C@C$, and $4W_2C@C/HTMs$ specimens measured in dark. (B) The current-time (i - t) curves of HTMs, $W_2C@C$ and $4W_2C@C/HTMs$ samples recorded under the light/off irradiation. (C) The EIS Nyquist plots and (D) the corresponding equivalent circuits of $W_2C@C$ (above), HTMs and $4W_2C@C/HTMs$ (below) photoelectrodes. (E) Normalized OCP decay profiles under light irradiation and in dark conditions, and (F) electron lifetime measurements derived from the OCP decay when the illumination is terminated over HTMs and $4W_2C@C/HTMs$ electrodes.

interface of HTMs and $W_2C@C$ maybe be one of the dominant factors for improving charge carrier separation. As for $W_2C@C$, the PL intensity is low may be caused by its nature character. Besides, to evaluate whether the surface area affects the photocatalytic activity, the Brunauer-Emmett-Teller (BET) analysis on HTMs, $W_2C@C$, $1W_2C@C/HTMs$ and $4W_2C@C/HTMs$ are carried out for comparison (Fig. S17). And the results indicate that the boosted photocatalytic activities of $W_2C@C/HTMs$ hybrids compared to pristine HTMs are not influenced by their surface areas.

3.3. Photo(electro)chemical measurements to expound the superiority of $W_2C@C/HTMs$ hybrid nanostructures

In order to have a comprehensive understand over the role of $W_2C@C$ in heterojunction, we characterize the obtained materials by a series of electrochemical and photoelectrochemical measurements. The current-voltage (LSV) plots of HTMs, $W_2C@C$, and $4W_2C@C/HTMs$ are examined for comparison, as displayed in Fig. 4A. As expected, $4W_2C@C/HTMs$ shows superior hydrogen evolution reaction (HER) activity in composition with pristine HTMs, because of the good HER performance of $W_2C@C$. As a matter of fact, the highly improved photocatalytic H_2 generation property of $4W_2C@C/HTMs$ with respect to pure HTMs could ascribe to the good

Electrochemical HER catalytic performance of $W_2C@C$ to some

extent, that providing active sites for H_2 reduction as well as boosting charge separation. Another important characterization for demonstrating the high-efficiency transfer and ultrafast charge separation in $W_2C@C/HTMs$ heterojunction is known as the current-time (i - t) curve obtained under chopped illumination (Fig. 4B). Notably, under a bias potential of 0.2 V vs. Ag/AgCl , the $4W_2C@C/HTMs$ photoelectrode generates the photocurrent density of $4 \mu\text{A cm}^{-2}$, nearly three times higher than the bare HTMs. For pristine $W_2C@C$, the value of photocurrent density is very low. It is reasonable to conclude that the incorporation of $W_2C@C$ on HTMs is essential to enhance the separation of photogenerated electron-hole pairs.

Further, we measure electrochemical impedance spectroscopy (EIS) to deduce the role of $W_2C@C$ in affecting the internal resistances for the charge transfer process in hybrids [32,33]. Fig. 4C shows the EIS spectra of HTMs, $W_2C@C$, and $4W_2C@C/HTMs$ photoelectrodes, which are performed under AM 1.5 G illumination at 0 V vs. Ag/AgCl and fitted by equivalent circuit models shown in Fig. 4D. In these two or three types of RC as illustrated in Fig. 4D, R_s usually represents the series resistance at the interface of the electrode and the FTO substrate, R_1 and R_2 are the resistance generally associated with the electron transport inside the electrode, and R_3 is identified as the charge transfer resistance at the electrode-electrolyte interface [34,35]. In Fig. 4C, we can observe that $4W_2C@C/HTMs$ shows the much smaller arcs than that of HTMs and the EIS fitting results are presented in Table S3. Thus,

we can acquire without a hitch that the values of R (refer to R_1 , R_2 and R_3) for $4W_2C@C/HTMs$ electrode are decreased compared with those in pure HTMs suggest that the highly efficient electron-hole separation responsible for PL quenching (Fig. 3F) and photocurrent increasing (Fig. 4B) could originate from the low charge transfer resistance. That is, the separation of photogenerated electron-hole pairs could be availablely achieved in $W_2C@C/HTMs$ heterojunction catalyst by rapidly transferring the charges to the surface active sites and effectively participating in the water reduction to generate H_2 . On the other hand, it is worth showing here that pure $W_2C@C$ shows very small resistance value (refer to R_2) for charge transfer (Table S4), during to its high conductive characteristic nature as well as the presence of carbon. Thus we ascribe the reduced charge transfer resistance in specimen of $W_2C@C/HTMs$ with respect to HTMs to the already formed heterojunction and the fast charge transfer rate in $W_2C@C$.

Besides, the open-circuit potential (OCP) decay transients of HTMs and $W_2C@C/HTMs$ are further conducted (Fig. S18), which carry information about the surface recombination [36,37]. The recombination of photogenerated electrons and holes can be defined according to Eq. 4 [36]:

$$\frac{V - V_{light}}{V_{dark} - V_{light}} = 1 - \exp(-kt) \quad (4)$$

in which V , V_{light} and V_{dark} represent the OCP values (V) at any time, under solar light irradiation and in dark, respectively, and k indicates the pseudo-first order recombination rate constant (s^{-1}). By plotting $\frac{V - V_{light}}{V_{dark} - V_{light}}$ against the time (t) for both bare HTMs and $4W_2C@C/HTMs$ (Fig. 4E), we observe that HTMs shows a rapidly decreased OCP profile than that of $4W_2C@C/HTMs$ hybrid. This result suggests that the surface recombination between trapped electrons and reaction intermediates in $W_2C@C/HTMs$ heterojunction is inhibited, that is to say much more effective charges are used to water reduction reaction. Further, the derivative profiles (Fig. 4F) from Fig. 4E could compare the electron lifetime of HTMs and $4W_2C@C/HTMs$ in qualitative. The decay lifetime of the accumulated electrons can be defined as Eq. (5) [38]:

$$\tau_n = \frac{k_B T}{e} \left(\frac{dOCP}{dt} \right)^{-1} \quad (5)$$

where τ_n represents the potential dependent lifetime, k_B stands for the Boltzmann's constant, T is the temperature in K, e indicates the charge of single electron, and OCP represents the open circuit potential at time t . As a result, the electron lifetime for $4W_2C@C/HTMs$ is significantly increased than that in bare HTMs demonstrates that the constructed heterojunction nanostructure could facilitate the separation of charge carriers, eventually promoting the electron transport process.

3.4. Photocatalytic mechanism for highly efficient water reduction

As is stated above, $W_2C@C$ shows positive roles in steering the behaviors of charge carriers in hybrids, such as accelerating their transfer, enhancing their separation as well as extending their lifetimes, all of which can make sure to finally achieve the significantly improved H_2 generation rate for heterojunction ($W_2C@C/HTMs$) photocatalysts with respect to pristine HTMs. Fig. 5A vividly illustrates the charge separation and transportation processes in $W_2C@C/HTMs$ heterojunction material under solar light irradiation. It can be clearly seen that the electrons and holes could be generated in HTMs when illuminated, electrons could be quickly transferred to the W_2C active sites through the conductive material of C shell, especially. While for the holes they show slow transfer rate, relatively speaking, since their large mass. As a result, the electron-hole pairs could be effectively separated in space, thus electron lifetime is significantly increased, eventually contributing to the high H_2 generation efficiency. On the calculated band structure results of bare HTMs and $W_2C@C$ from UV-vis DRS and UPS

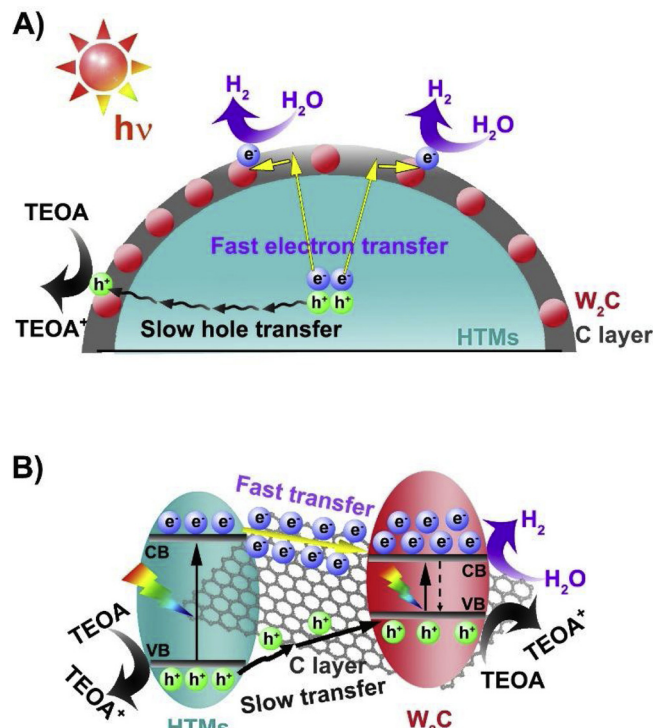


Fig. 5. (A) Schematic illustration of the charge transfer and separation in $W_2C@C/HTMs$ hybrid under simulated solar light irradiation. (B) Schematic electronic band structure and photocatalytic mechanism for water reduction.

measurements (Fig. 3C–E), the schematic mechanism underlying the photogenerated carrier behaviors (generation, separation, transportation as well as surface reactions) involved in the system is provided, as shown in Fig. 5B. Clearly, type I heterojunction [39] is formed when HTMs and $W_2C@C$ are integrated together and an internal electric field could be formed at their contact interface [10]. Under solar light illumination, both HTMs and W_2C can be excited to generate electrons and holes, then CB-electrons of HTMs are injected into the CB of W_2C while VB of W_2C also accepts the holes coming

from HTMs, which a charge transfer process seems to result in their recombination. But, considering the different transfer rates of electrons and holes as well as the existing internal electric field, it is not the fact. Apparently, CB of W_2C could be collected much more electrons from CB of HTMs through charge-transfer channel of C, and meanwhile, the potential of E_{CB} for $W_2C@C$ is -0.42 V vs. NHE, which is well above $E(H^+/H_2, 0$ V vs. NHE). As such, CB-electrons of W_2C could be employed to reduce H^+ to generate H_2 . As for both the small amount of holes trapped by VB of W_2C and the holes in VB of HTMs, they can be quickly consumed by sacrificial agent of TEOA owing to the high hole harvesting ability, to obtain TEOA^{*}. In such a way, the whole charge kinetics in our constructed $W_2C@C/HTMs$ heterojunction certainly result in substantial charge separation. That is, because of the cocatalysis effect of W_2C and excellent conductivity of carbon, the introduction of $W_2C@C$ can function as an electron collector and transporter in the hybrid that strongly pull electrons escaping from the CB of HTMs and eliminate the charge recombination possibility in bare HTMs, leading to a huge enhancement in the photocatalytic activity for H_2 generation.

4. Conclusions

In summary, the $W_2C@C/HTMs$ heterojunction nanostructures are successfully constructed and reported for the first time by coating C supported W_2C NPs on TiO_2 hollow microspheres, acting as one highly active material for photocatalytic H_2 generation from water reduction. The introduction of $W_2C@C$ endows the hybrid photocatalyst with

several good characters, including the enhanced light absorption capability, rapid charge transfer rate, efficient spatial charge separation, as well as the abundant and accessible reaction sites. Under solar light irradiation, a dramatically enhanced H₂ generation rate of 6.91 mmol h⁻¹ g⁻¹ is achieved for 4W₂C@C/HTMs, which is 21 times that of bare HTMs. Therefore, this work paves the way toward designing functional materials with efficient structures for promoting solar-light-driven H₂ generation.

Acknowledgments

This work was financially supported by the Support Plan for College Science and Technology Innovation Team of Henan Province (No. 16IRTSTHN001), the Science & Technology Innovation Talent Plan of Henan Province (No. 174200510018) and the Outstanding Talent Research Fund of Zhengzhou University (32310149, 32310198 and 32310222), and Postdoctoral Science Foundation (1901006, 2019M652570 and 2019M650172).

Appendix A. Supplementary data

Supplementary material related to this article can be found, in the online version, at doi:<https://doi.org/10.1016/j.apcatb.2019.117760>.

References

- [1] Y. Tachibana, L. Vayssières, J.R. Durrant, *Nat. Photonics* 6 (2012) 511–518.
- [2] C. Huang, C. Chen, M. Zhang, L. Lin, X. Ye, S. Lin, M. Antonietti, X. Wang, *Nat. Commun.* 6 (2015) 7698.
- [3] S.-S. Yi, X.-B. Zhang, B.-R. Wulan, J.-M. Yan, Q. Jiang, *Energy Environ. Sci.* 11 (2018) 3128–3156.
- [4] A. Fujishima, K. Honda, *Nature* 238 (1972) 37–38.
- [5] X. Liu, G. Zhu, X. Wang, X. Yuan, T. Lin, F. Huang, *Adv. Energy Mater.* 6 (2016) 1600452.
- [6] F. Ning, M. Shao, S. Xu, Y. Fu, R. Zhang, M. Wei, D.G. Evans, X. Duan, *Energy Environ. Sci.* 9 (2016) 2633–2643.
- [7] H.-A. Park, S. Liu, Y. Oh, P.A. Salvador, G.S. Rohrer, M.F. Islam, *ACS Nano* 11 (2017) 2150–2159.
- [8] L. Guo, Z. Yang, K. Marcus, Z. Li, B. Luo, L. Zhou, X. Wang, Y. Du, Y. Yang, *Energy Environ. Sci.* 11 (2018) 106–114.
- [9] H. Gong, Q. Liu, C. Huang, *Int. J. Hydrogen Energy* 44 (2019) 4821–4831.
- [10] S. Bai, J. Jiang, Q. Zhang, Y. Xiong, *Chem. Soc. Rev.* 44 (2015) 2893–2939.
- [11] S.P. Berglund, H. He, W.D. Chemelewski, H. Celio, A. Dolocan, C.B. Mullins, *J. Am. Chem. Soc.* 136 (2014) 1535–1544.
- [12] Q. Gong, Y. Wang, Q. Hu, J. Zhou, R. Feng, P.N. Duchesne, P. Zhang, F. Chen, N. Han, Y. Li, C. Jin, Y. Li, S.-T. Lee, *Nat. Commun.* 7 (2016) 13216.
- [13] M. Zeng, Y. Chen, J. Li, H. Xue, R.G. Mendes, J. Liu, T. Zhang, M.H. Ruemmel, L. Fu, *Nano Energy* 33 (2017) 356–362.
- [14] Z. Liping, Y. Hongbin, D.K.J.A. Wanigarathna, L. Bin, *Small Methods* 2 (2018) 1700353.
- [15] X. Yue, S. Yi, R. Wang, Z. Zhang, S. Qiu, *Nano Energy* 47 (2018) 463–473.
- [16] M.-H. Sun, S.-Z. Huang, L.-H. Chen, Y. Li, X.-Y. Yang, Z.-Y. Yuan, B.-L. Su, *Chem. Soc. Rev.* 45 (2016) 3479–3563.
- [17] T. Ohsaka, F. Izumi, Y. Fujiki, *J. Raman Spectrosc.* 7 (1978) 321–324.
- [18] Y. Peng, K. Li, J. Li, *Appl. Catal. B: Environ.* 140 (2013) 483–492.
- [19] L.-N. Zhang, Y.-Y. Ma, Z.-L. Lang, Y.-H. Wang, S.U. Khan, G. Yan, H.-Q. Tan, H.-Y. Zang, Y.-g. Li, J. Mater. Chem. A 6 (2018) 15395–15403.
- [20] Y.-T. Xu, X. Xiao, Z.-M. Ye, S. Zhao, R. Shen, C.-T. He, J.-P. Zhang, Y. Li, X.-M. Chen, *J. Am. Chem. Soc.* 139 (2017) 5285–5288.
- [21] Y. Wang, D.C. Alsmeyer, R.L. McCreery, *Chem. Mater.* 2 (1990) 557–563.
- [22] J. Hou, S. Cao, Y. Sun, Y. Wu, F. Liang, Z. Lin, L. Sun, *Adv. Energy Mater.* (2017) 1701114.
- [23] C.K. Poh, S.H. Lim, Z. Tian, L. Lai, Y.P. Feng, Z. Shen, J. Lin, *Nano Energy* 2 (2013) 28–39.
- [24] X. Zhao, J. Feng, J. Liu, J. Lu, W. Shi, G. Yang, G. Wang, P. Feng, P. Cheng, *Adv. Sci.* 5 (2018) 1700590.
- [25] Y. Liu, B. Zhang, L. Luo, X. Chen, Z. Wang, E. Wu, D. Su, W. Huang, *Angew. Chem. Int. Ed.* 54 (2015) 15260–15265.
- [26] Z. Zhang, Y. Huang, K. Liu, L. Guo, Q. Yuan, B. Dong, *Adv. Mater.* 27 (2015) 5906–5914.
- [27] Y.-P. Yuan, L.-W. Ruan, J. Barber, S.C.J. Loo, C. Xue, *Energy Environ. Sci.* 7 (2014) 3934–3951.
- [28] S.-S. Yi, J.-M. Yan, B.-R. Wulan, S.-J. Li, K.-H. Liu, Q. Jiang, *Appl. Catal. B: Environ.* 200 (2017) 477–483.
- [29] Y. Wang, X. Liu, J. Liu, B. Han, X. Hu, F. Yang, Z. Xu, Y. Li, S. Jia, Z. Li, Y. Zhao, *Angew. Chem. Int. Ed.* 57 (2018) 5765–5771.
- [30] Z. Cheng, T.A. Shifa, F. Wang, Y. Gao, P. He, K. Zhang, C. Jiang, Q. Liu, J. He, *Adv. Mater.* 30 (2018) 1707433.
- [31] J. Liu, Y. Liu, N. Liu, Y. Han, X. Zhang, H. Huang, Y. Lifshitz, S.-T. Lee, J. Zhong, Z. Kang, *Science* 347 (2015) 970–974.
- [32] F.-M. Zhang, J.-L. Sheng, Z.-D. Yang, X.-J. Sun, H.-L. Tang, M. Lu, H. Dong, F.-C. Shen, J. Liu, Y.-Q. Lan, *Angew. Chem. Int. Ed.* 57 (2018) 12106–12110.
- [33] Q. Liu, C. Chen, M. Du, Y. Wu, C. Ren, K. Ding, M. Song, C. Huang, *ACS Appl. Nano Mater.* 1 (2018) 4566–4575.
- [34] Y.-F. Xu, X.-D. Wang, H.-Y. Chen, D.-B. Kuang, C.-Y. Su, *Adv. Funct. Mater.* 26 (2016) 4414–4421.
- [35] E.S. Kim, N. Nishimura, G. Magesh, J.Y. Kim, J.-W. Jang, H. Jun, J. Kubota, K. Domen, J.S. Lee, *J. Am. Chem. Soc.* 135 (2013) 5375–5383.
- [36] H.-i. Kim, D. Monllor-Satoca, W. Kim, W. Choi, *Energy Environ. Sci.* 8 (2015) 247–257.
- [37] Z. Hu, Z. Shen, J.C. Yu, *Chem. Mater.* 28 (2016) 564–572.
- [38] B.H. Meekins, P.V. Kamat, *ACS Nano* 3 (2009) 3437–3446.
- [39] S.J.A. Moniz, S.A. Shevlin, D.J. Martin, Z.-X. Guo, J. Tang, *Energy Environ. Sci.* 8 (2015) 731–759.